International Journal of Aeronautical and Space Sciences (2026) 27:2245–2263
https://doi.org/10.1007/s42405-025-01084-5

ORIGINAL PAPER

Mid-Fidelity Aeroelastic Framework for Main Rotor Load Prediction in Forward Flight of Medium Utility Helicopters

Inho Jeong[1] · Sa-Lang Lee[2] · Hakjin Lee[2] · Wooram Kang[3] · Jae-Sang Park[4] · Haeseong Cho[1,5,6]

Received: 11 July 2025 / Revised: 13 October 2025 / Accepted: 9 November 2025 / Published online: 28 November 2025

Abstract

Rotorcraft in forward flight exhibit complex aeroelastic interactions owing to the coupling of unsteady aerodynamics with structural flexibility. This study presents a mid-to-high-fidelity aeroelastic framework for a medium-utility helicopter, integrating a nonlinear vortex-lattice method/vortex particle method (NVLM/VPM) aerodynamic solver with geometrically exact beam theory (GEBT) for rotor blade dynamics. The framework captures full geometric nonlinearity and inertial coupling, with a loosely coupled δ-airload scheme linking aerodynamics and the structural response at each trim state. Simulations at 40, 100, and 140 knots demonstrate good agreement with the CAMRAD II results, validating the accuracy of the wake-resolved aerodynamics and nonlinear blade dynamics. The results show that the proposed GEBT–NVLM framework offers a reliable research tool for accurate aeroelastic load prediction and early-phase evaluation of active control strategies.

Keywords Geometrically exact beam theory · Nonlinear vortex-lattice method · Vortex particle method · Aeroelastic analysis · Rotorcraft comprehensive code

1 Introduction

Rotorcraft rotors generate thrust and control forces simultaneously, and their blades are continually exposed to inertial, elastic, and aerodynamic forces that interact in a highly nonlinear manner. In forward flight, the asymmetric inflow caused by blade-vortex interaction (BVI), wake interference, and fuselage effects produces unsteady loads that translate into vibration, noise, and fatigue. Operational experience has demonstrated that such vibrations can accelerate structural wear and increase maintenance costs, making vibration reduction a critical design objective [1].

Active technologies such as higher harmonic control (HHC), individual-blade control (IBC), and active twist rotor (ATR) seek to mitigate vibrations by altering the unsteady aerodynamic loads on each blade [2]. Effective implementation demands an aeroelastic tool that delivers hub-load amplitude and phase with high accuracy over a wide advance-ratio range, with fidelity that conventional lifting-line codes struggle to maintain under a large forward-speed parameter.

On the computational side, Wang et al. used a free-wake model coupled with three-dimensional (3D) finite elements (FEs) and validated the results against flight data [3], while Huang et al. introduced preCICE-based coupling and verified a panel-method solver against CAMRAD II [4]. Hybrid approaches combining panel-plus-free-wake aerodynamics with 3D FE structures [5] and unsteady vortex-lattice methods (UVLMs) for blade dynamics [6] have also been reported. For the HART II rotor, Kang et al. performed a loose coupling and showed that sectional loads were more

Communicated by Joong-Kwan Kim.

†Inho Jeong and Sa-Lang Lee have contributed equally to this work.

✉ Haeseong Cho
hcho@jbnu.ac.kr

1 Department of Aerospace Engineering, Jeonbuk National University, Jeonju 54896, Republic of Korea

2 School of Aerospace Engineering, Gyeongsang National University, Jinju 52828, Republic of Korea

3 Rotary-Wing Flight Dynamics Team, Korea Aerospace Industries, Sacheon 52529, Republic of Korea

4 Department of Aerospace Engineering, Chungnam National University, Daejeon 34134, Republic of Korea

5 Graduate School of Mechanical-Aerospace-Electric Convergence Engineering, Jeonbuk National University, Jeonju 54896, Republic of Korea

6 Future Air Mobility Research Center, Jeonbuk National University, Jeonju 54896, Republic of Korea

sensitive to grid resolution than to time step, underscoring the need for surface-resolved aerodynamics [7]. Additional threads have explored material property effects [8], model order reduction [9], and eVTOL configurations [10]. On the control/operations side, Park et al. demonstrated simultaneous vibration alleviation and performance gains via multi-harmonic individual-blade control [11]. Chen et al. devised a dynamic take-off/landing controller for multi-rotor eVTOL configurations [12], and Bhalla et al. showed that control-moment gyroscopes can improve passenger comfort by attenuating cabin vibration [13]. On the experimental side, Wernicke [14] and Splettstoesser et al. [15, 16] demonstrated hub-load reduction using HHC, while Bang et al. [17] and Hong et al. [18] simulated HHC or IBC with CAMRAD II. Lim et al. evaluated 2GCHAS for BVI loads but noted limitations owing to its free-wake model [19].

Despite these advances, widely used comprehensive codes, i.e., CAMRAD II [20], DYMORE [21], and RCAS [22], still depend on lifting-line aerodynamics and free-wake inflow. Their displacement-based geometrically exact beams (GEBT) require extra post-processing to retrieve internal forces, and the default aerodynamics lack the geometric fidelity needed for blades with sweep, taper, or advanced airfoils. Hodges [23] addressed part of this gap by introducing a mixed-variational GEBT that computes displacements and internal forces simultaneously; this formulation has since been adopted in RCAS and other applications [20]. Nevertheless, most platforms still rely on low-order inflow models that cannot resolve wake curvature or reverse-flow effects at high advance ratio.

Thus, the relevant limitation is a transparent, mid-fidelity workflow that (i) resolves blade-surface aerodynamics and geometrically exact elastic coupling, (ii) predicts trimmed hub-load amplitude and phase across advance ratio, and (iii) remains practical for forward-flight vibration assessment and design-loop studies. Full CFD/CSD coupling can meet accuracy needs but is often impractical for routine use; conversely, low-order comprehensive tools are efficient but struggle with wake curvature and reverse-flow physics at higher advance ratios.

To address these needs, this study presents a modular, mid-fidelity framework that couples a surface-resolved aerodynamic solver, such as the nonlinear vortex-lattice method (NVLM) with vortex particle method (VPM) wake tracking, to a mixed-variational GEBT structural model via a δ-airload loose-coupling scheme. The aerodynamic module predicts unsteady sectional airloads and resolves 3D wake evolution without relying on prescribed inflow models, while the structural solver retains full large-deflection kinematics and inertial coupling. The approach is demonstrated on a four-bladed main rotor at 40, 100, and 140 knots. By combining transparent model access and physics-resolved wake–structure interaction, the proposed GEBT–NVLM framework offers a reliable approach for aeroelastic load assessment of a helicopter main rotor, sensitivity studies, and early-stage active control evaluation.

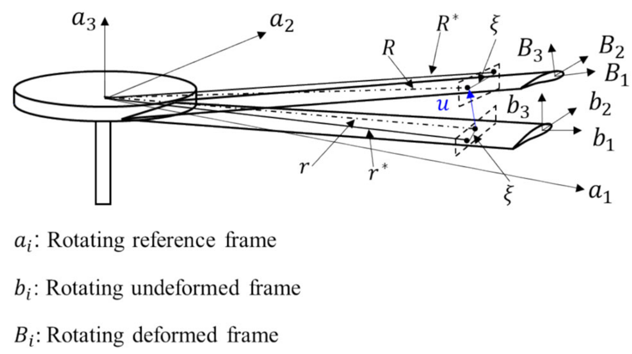

Fig. 1 Rotating frames used in the GEBT

2 Aeroelastic Analysis Using GEBT and Lifting-Line Theory

2.1 GEBT

The rotor blade deformation was predicted using a mixed-variational GEBT. Three orthonormal frames were employed (Fig. 1): a rotating a-frame attached to the hub, an undeformed b-frame coinciding with the initial geometry of the blade, and a deformed B-frame representing the current configuration. The displacements and finite rotations were expressed in the a-frame, whereas the strains, internal forces, velocities, and momentum were evaluated in the B-frame; the intervening b-frame provided the reference shape from which the large-deflection kinematics were measured. This three-frame arrangement preserved full geometric nonlinearity while keeping the constitutive relations and dynamic balance equations compact.

The mixed-variational formulation based on the GEBT was derived from Hamilton's principle, as follows:

$$\int_{t_1}^{t_2} \int_0^l \left[\delta(K - U) + \overline{\delta W}\right] \mathrm{d}x_1 \mathrm{d}t = \overline{\delta A}, \tag{1}$$

where t denotes time and l represents the blade length. K and U are the kinetic and strain energies, respectively. $\overline{\delta W}$ and $\overline{\delta A}$ denote the virtual work and the virtual displacement at the blade ends due to external loads, respectively. $\overline{(\cdot)}$ indicates that the corresponding quantity is not a variation of a function.

The strain- and velocity-related quantities that satisfy the geometrically exact conditions proposed by Hodges [23] are defined as follows:

$$\begin{aligned}
\gamma^* &= C^{Ba}\left(C^{ab}e_1 + u_a'\right) - e_1,\\
\kappa^* &= C^{ba}T_s(\theta)\theta',\\
V_B^* &= C^{Ba}(v_a + \dot{u}_a + \tilde{\omega}_a u_a) - e_1,\\
\Omega_B^* &= C^{ba}T_s(\theta)\dot{\theta} + C^{Ba}\omega_a,
\end{aligned} \tag{2}$$

where the superscript $(\bullet)^*$ indicates that the quantity satisfies the geometrically exact condition.

To enforce the geometrically exact constraint, a Lagrange multiplier was introduced to Eq. (1), resulting in the following complete mixed-variational formulation:

$$\begin{aligned}
&\int_{t_1}^{t_2}\int_0^l \Big[\delta V_B^{*T} P_B + \delta\Omega_B^{*T} H_B - \delta\gamma^{*T} F_B - \delta\kappa^{*T} M_B\\
&+ \delta F_B^T\left(\gamma - \gamma^*\right) + \delta M_B^T\left(\kappa - \kappa^*\right) - \delta P_B^T\left(V_B - V_B^*\right)\\
&- \delta H_B^T\left(\Omega_B - \Omega_B^*\right)\Big]\mathrm{d}x_1\mathrm{d}t + \int_{t_1}^{t_2}\int_0^l \overline{\delta W}\mathrm{d}x_1\mathrm{d}t = \overline{\delta A}.
\end{aligned} \tag{3}$$

By expressing the variations in each physical quantity and applying FE discretization, the following weak form was obtained in the a-frame:

$$\int_{t_1}^{t_2} \sum_i^N \delta\Pi_i \mathrm{d}t = 0. \tag{4}$$

Each beam element employs linear Lagrange (C^0) shape functions $N_1 = 1 - s/L_e,\ N_2 = s/L_e$ for all intrinsic GEBT state fields; rotations are parameterized via the exponential map and interpolated at the parameter level. Using linear shape functions and approximations [24], Eq. (4) can be rewritten as follows:

$$\int_{t_1}^{t_2} \delta X^T\left[F_s\left(X, \dot{X}\right)\right]\mathrm{d}t = 0, \tag{5}$$

where F_s is the structural operator and X is the structural state vector that includes displacements, rotations, internal forces, and momentum. The nonlinear structural equilibrium equation is expressed as follows:

$$F_s\left(X, \dot{X}\right) = 0. \tag{6}$$

Applying the Newton–Raphson method to Eq. (6) yields

$$\left[\frac{\partial F_S}{\partial X}_{\mathrm{eff}}\right]\Delta X = \Delta R,\ \ \Delta R = F_{\mathrm{ext}} - F_S(X). \tag{7}$$

The effective Jacobian is given by

$$\frac{\partial F_S}{\partial X}_{\mathrm{eff},i} = \frac{\partial F_S}{\partial X}_i + \frac{1}{\beta\Delta t}\frac{\partial F_S}{\partial \dot{X}}_i. \tag{8}$$

The structural state vector was updated using the Newmark-β method. Once the residual force converged, the analysis proceeded to the next time step. Consequently, the displacements, rotations, internal forces, and momentum of the rotor blade were computed over time. In addition, the velocity and acceleration responses of the structures were obtained.

2.2 Two-Dimensional (2D) Unsteady Lifting-Line Theory

An unsteady 2D lifting-line theory that extended the classical Theodorsen approach with the linear inflow model of White and Blake was employed for aeroelastic analysis. The sectional relative velocity in the deformed blade frame B was obtained by a double rotation of the free-stream and structural motion terms, as follows:

$$U = C^{Ba}\left(C^{ai}V_\infty + \lambda_i e_3 - C^{aB}V_B\right), \tag{9}$$

where C^{ai} is the rotation from the inertial frame to the rotating reference frame a, V_∞ is the free-stream velocity vector, $\lambda_i e_3$ is the axial induced inflow, and V_B is the sectional velocity generated by blade spin and structural deformation. The induced inflow coefficient λ_i follows the White–Blake linear model, expressed in non-dimensional form as follows:

$$\lambda_i = \lambda_0\left(\kappa_x r\cos(\psi_{azi}) + \kappa_y r\sin(\psi_{azi})\right),\ \ \lambda_0 = \Omega R\sqrt{\left(\frac{C_T}{2}\right)}, \tag{10}$$

with advance ratio-dependent factors:

$$\kappa_x = \sqrt{2}\frac{\mu}{\sqrt{\mu^2 + \lambda_i^2}},\ \ \kappa_y = -2\mu. \tag{11}$$

Once the local inflow was determined, the static lift L^s, drag D^s, and quarter-chord pitching moment M^s were directly obtained from the 2D airfoil coefficients:

$$\begin{aligned}
L^{\mathrm{s}} &= c_\ell(\alpha, \mathcal{M})\rho b V U_2,\\
D^{\mathrm{s}} &= c_\ell(\alpha, \mathcal{M})\rho b V U_3,\\
M_{\mathrm{qc}}^{\mathrm{s}} &= c_m(\alpha, \mathcal{M})2\rho b^2 V^2.
\end{aligned} \tag{12}$$

Unsteady increments L^{us} and M^{us} were then added to account for the pitch-rate effects and the additional normalwash generated by flapwise acceleration:

$$\begin{aligned}
L^{\mathrm{us}} &= a_0\rho b^2 U_2\omega_1 - a_0\rho\frac{b^2}{2}\dot{v}_{a3},\\
M_{\mathrm{qc}}^{\mathrm{us}} &= -a_0\rho\frac{b^4}{16}\dot{\omega}_1 - \frac{b}{2}L^{\mathrm{us}}.
\end{aligned} \tag{13}$$

The remaining terms S_1, S_2, S_3 represent the viscous and pressure-drag corrections:

$$\begin{aligned} S_1 &= c_{d0}(\alpha, \mathcal{M})\rho b V_R U_1, \\ S_2 &= c_d(\alpha, \mathcal{M})\rho b V U_2 + c_{d0}(\alpha, \mathcal{M})\rho b (V_R - U_2) U_2, \\ S_3 &= c_d(\alpha, \mathcal{M})\rho b V U_3. \end{aligned} \tag{14}$$

The complete sectional force and moment vectors in the deformed blade frame B are as follows:

$$f_B = \begin{Bmatrix} S_1 \\ D^s - S_2 \\ L^s + L^{us} + S_3 \end{Bmatrix}, \quad m_B = \begin{Bmatrix} M^s + M^{us} \\ 0 \\ 0 \end{Bmatrix}, \tag{15}$$

where zero entries in m_B denote the absence of spanwise twisting and lagwise aerodynamic moments in the lifting-line approximation.

Before these loads could be applied to the GEBT, they were interpolated from the sectional grid to the GEBT nodal points and rotated back into the rotating reference frame a:

$$f_a = C^{aB} f_B, \;\; m_a = C^{aB} m_B. \tag{16}$$

The nodal vectors f_a and m_a were then introduced as external forces in the structural residuals $F_s\left(X, \dot{X}\right)$.

2.3 Trim Analysis

Once the target thrust, rolling, and pitching moments were determined, the collective pitch θ_0 and the cyclic pitch θ_{1s}, θ_{1c} were changed and aero-structural coupled analysis was performed to derive the thrust, rolling, and pitching moments for one revolution. The analysis was performed until the difference between the target and derived values was within the desired level. The pitch input for each revolution was calculated as follows:

$$\begin{aligned} \theta_{t+1} &= \theta_t + \Delta t J^{-1}\left(y^{\text{Target}} - y_{t+1}\right), \\ y^{\text{Target}} &= \left[y_1^{\text{Target}}, y_2^{\text{Target}}, \ldots, y_{N_i}^{\text{Target}}\right], \end{aligned} \tag{17}$$

where y^{Target} corresponds to the target output and y_{t+1} is the output derived through the calculation.

J is the Jacobian matrix for the input and output used in the trim analysis and was calculated as follows:

$$J = \frac{\partial y}{\partial \theta} = \left[\frac{y_1 - y_1^{\text{Ref}}}{\Delta_1}, \frac{y_2 - y_2^{\text{Ref}}}{\Delta_2}, \ldots, \frac{y_{N_i} - y_{N_i}^{\text{Ref}}}{\Delta_{N_i}}\right], \tag{18}$$

where y_i^{Ref} is the output calculated based on the reference input, Δ_i is the perturbation, and y_i is the output in the input with the perturbation. Trim analysis in forward flight was performed using an automatic control routine, referred to as an auto-pilot-based trim procedure.

3 Extended Aeroelastic Analysis with NVLM/VPM

3.1 Nonlinear Vortex Lattice Method (NVLM)

In this study, a NVLM was used as an aerodynamic model for the developed aeroelastic analysis code. This method efficiently determines the aerodynamic loads on rotor blades in an incompressible flow while maintaining computational efficiency. Unlike lifting-line theory, which is widely used in comprehensive rotorcraft analysis codes, the present NVLM formulation enables both spanwise and chordwise discretization with vortex ring elements distributed along the camber surface, providing a more detailed geometric representation, including dihedral angles, cambers, and sweep. However, sweep effects are only partially captured through their influence on the induced flow distribution, as explicit spanwise cross-flow modeling is not included. Moreover, this method inherently excludes explicit airfoil thickness modeling. The aerodynamic influence of thickness is instead incorporated indirectly through airfoil data tables. In addition, this approach incorporates an airfoil look-up table, vortex strength correction, and correction functions of aerodynamic coefficients to account for the nonlinear aerodynamic characteristics induced by viscous effects [25, 26]. The strength (Γ) of the discretized vortex ring element for the rotor blade was determined using Eq. (19). The influence coefficients (a_{ij}) representing the velocity components induced by the vortex ring element at the collocation points perpendicular to the grid are expressed by Eq. (20). The right-hand side (RHS) term in Eq. (21) represents the axial components of the free-stream velocity, the wake-induced velocity, and the velocity component associated with rotor rotation:

$$\begin{bmatrix} a_{11} & a_{12} & \cdots & a_{1m} \\ a_{21} & a_{22} & \cdots & a_{2m} \\ \vdots & \vdots & \ddots & \vdots \\ a_{k1} & a_{k2} & \cdots & a_{km} \end{bmatrix} \begin{Bmatrix} \Gamma_1 \\ \Gamma_2 \\ \vdots \\ \Gamma_m \end{Bmatrix} = \begin{Bmatrix} \text{RHS}_1 \\ \text{RHS}_2 \\ \vdots \\ \text{RHS}_k \end{Bmatrix} \tag{19}$$

$$a_{ij} = (\boldsymbol{V}_{\text{ind, bound}})_{ij} \cdot n_i \tag{20}$$

$$\text{RHS}_i = -(\boldsymbol{V}_\infty + \boldsymbol{V}_{\text{ind, wake}} - \Omega \times r)_i \cdot n_i \tag{21}$$

Once the strength of the vortex ring element was determined by solving a linear system of equations, the rotor

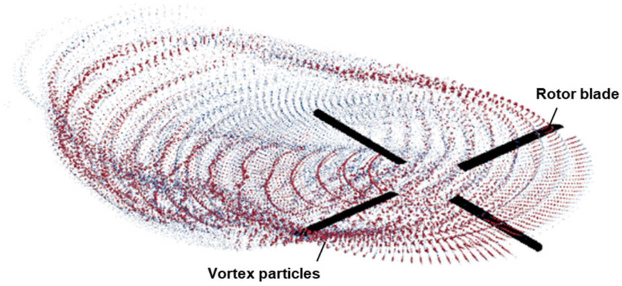

Fig. 2 Vortex particles shed from the rotor blades and forming a helical wake structure

wake strength could be calculated using the Kutta condition. To calculate the aerodynamic loads acting on the rotor blades through a table look-up approach, the sectional flow conditions including local inflow velocity (V_{inflow}) and effective angle of attack (α_{eff}) at each spanwise location were determined. The inflow velocity at each rotor blade sectional position was computed using Eq. (22). After determining the inflow velocity, the effective angle of attack could be obtained using Eq. (23):

$$\boldsymbol{V}_{\text{inflow}} = \boldsymbol{V}_{\infty} - \Omega \times r + \boldsymbol{V}_{\text{ind, bound}} + \boldsymbol{V}_{\text{ind, wake}}, \tag{22}$$

$$\alpha_{\text{eff}} = \theta_{\text{twist}} + \theta_{\text{pitch}} + \tan^{-1}\left(\frac{\boldsymbol{V}_{\text{inflow}} \cdot \boldsymbol{a}_3}{\boldsymbol{V}_{\text{inflow}} \cdot \boldsymbol{a}_1}\right). \tag{23}$$

The local twist and blade pitch angles are indicated by θ_{twist} and θ_{pitch}, respectively, while the unit tangential and normal vectors to the rotor disc plane are indicated by $\boldsymbol{a}_1$ and $\boldsymbol{a}_3$, respectively. Consequently, the lift, drag, and moment coefficients of the airfoil at each sectional position could be determined based on the effective angle of attack, Mach number, or Reynolds number [27, 28].

3.2 Vortex Particle Method (VPM)

In this study, the rotor wake was modeled using the vortex particle method (VPM), a Lagrangian-based approach that represents the wake as a collection of discrete vortex particles. Unlike filament-based free-wake methods, VPM does not impose topological connectivity between neighboring wake elements, offering greater numerical flexibility in capturing complex vortex dynamics such as roll-up, interaction, and breakdown. Figure 2 shows a representative schematic of the VPM framework, where the rotor blades shed vortex particles that evolve freely in space to form the helical wake. Each vortex particle convects independently in the flow field, interacting dynamically with all other particles. As shown in Fig. 2, the wake exhibits coherent tip-vortex structures and complex interaction patterns, which can be accurately resolved using the VPM formulation. This approach enables accurate prediction of self-induced wake deformation and

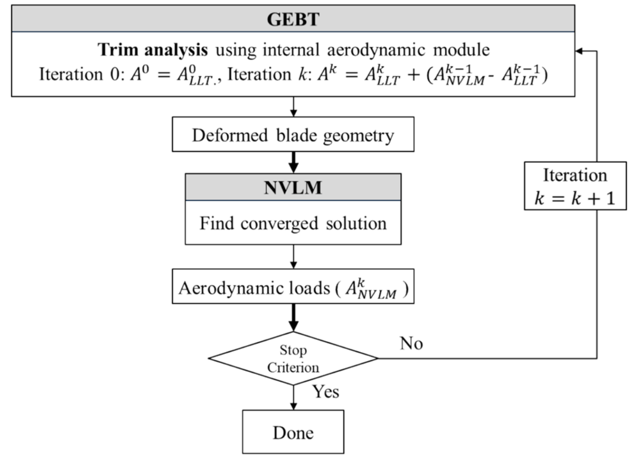

Fig. 3 Flow chart of aero-structure coupled analysis with δ-airload coupling

rotor–wake interaction phenomena in rotorcraft without relying on grid-based solvers. It is particularly well suited for capturing unsteady blade loading and blade–vortex interactions (BVI).

The velocity components induced by the rotor wake, modeled as discrete vortex particles, were determined as follows:

$$\boldsymbol{u}(\boldsymbol{x}_i, t) = -\sum_{j=1}^{\rho} \frac{1}{\sigma_{ij}^3} K(\rho)(\boldsymbol{x}_i - \boldsymbol{x}_j) \times \alpha_j, \tag{24}$$

where ρ is the dimensionless distance parameter and σ is the core radius of vortex particles. $K(\sigma)$ is the normalized kernel function, which is defined using Green's function. To prevent singularities and numerical instability using the Biot–Savart law, a regularized kernel function was used to distribute the vorticity over a finite region, as follows:

$$K(\rho) = \frac{G(\rho) - \xi(\rho)}{\rho}. \tag{25}$$

This formulation ensures smooth velocity induction and improves the numerical stability of the wake structure evolution. A detailed description of the numerical strategy for wake modeling is provided in Refs. [29, 30].

3.3 Loosely Coupled Approach via δ-Airload Method

The aero-structure coupled analysis in this study employed the δ-airload method, a loosely coupled technique that facilitates iterative convergence between aerodynamic and structural solvers. The computational procedure for the developed forward-flight aeroelastic analysis framework is shown in Fig. 3.

Initially, an undeformed rotor blade configuration, neglecting the structural deformation, was modeled within the aerodynamic module. A trim analysis was performed

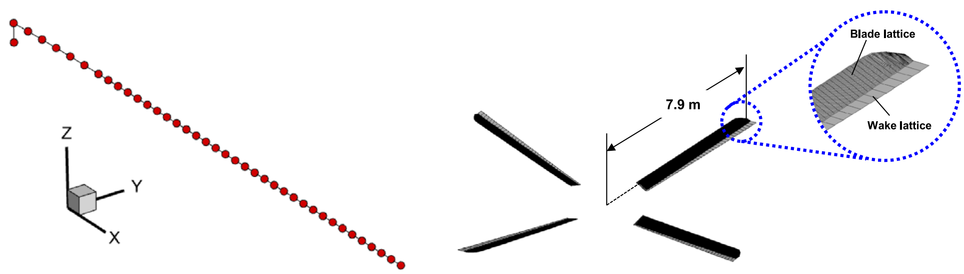

(a) Beam-element discretization (b) NVLM lattice

Fig. 4 Structural and aerodynamic representations of the main rotor blades

under this configuration to obtain the aerodynamic loads $A^{(0)}_{\mathrm{NVLM}}$, which are defined as spanwise distributed six-component forces that vary with the azimuth angle. These loads were then passed to the structural solver, which performed a separate trim analysis based on lifting-line theory to compute the internal aerodynamic forces $A^{(0)}_{\mathrm{LLT}}$.

The δ-airload, defined as the difference between external and internal aerodynamic loads, is expressed as follows:

$$\Delta A^0 = A^{(0)}_{\mathrm{NVLM}} - A^{(0)}_{\mathrm{LLT}} \tag{26}$$

and was used to correct the internal airloads during structural trimming. Therefore, the total aerodynamic load at iteration k is expressed as follows:

$$A^k = A^k_{\mathrm{LLT}} + \left(A^{k-1}_{\mathrm{NVLM}} - A^{k-1}_{\mathrm{LLT}}\right). \tag{27}$$

After solving the structural response under the corrected aerodynamic load, the updated blade deformation and control angles were fed back into the aerodynamic solver, which computed the revised aerodynamic loads for the next iteration. The sequence of computations constituted a single coupled iteration. Except for the initial undeformed rotor case, trim analysis was performed within the structural module in all subsequent iterations, allowing for faster convergence compared with aerodynamic-module-based trimming. Through repeated iterations, the control angles and blade deformation converged and the final solution accurately reflected the aerodynamic characteristics predicted by the high-fidelity NVLM-based model within the coupled aeroelastic analysis.

4 Numerical Results of Main Rotor Load Analysis

A medium-utility helicopter was used as the target configuration to verify the developed aero-structural coupling analysis model for forward flight. The main rotor, which was equipped with an articulated hub, consisted of four blades. The geometric and physical properties used in the modeling were based on data provided by the manufacturer. As shown in Fig. 4, an aerodynamic grid for the rotor blades was constructed using 15 divisions in the chordwise direction and 20 divisions in the spanwise direction after grid-convergence study. The blade was discretized with 41 geometrically exact beam elements, matching the 41 spanwise property stations provided by the manufacturer (authors). The global state vector has size $n_X = 18\,N_e + 12$, which gives $n_X = 750$ for $N_e = 41$.

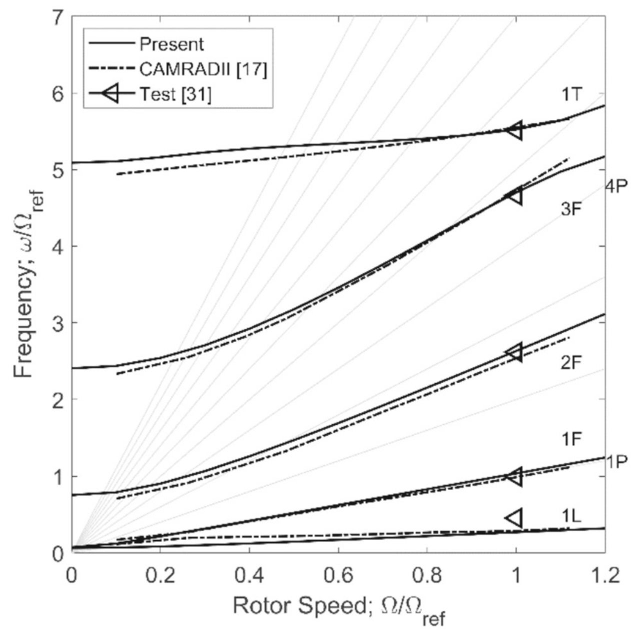

Fig. 5 Fan diagram of the medium-utility helicopter main rotor blade

Prior to the coupled aero-structural analysis, a modal analysis was performed and compared with previously published results [17] and experimental data [31], as shown in Fig. 5. The comparison included the first five modes and demonstrated good agreement in both the mode shapes and natural frequencies. For a four-bladed rotor, the primary excitation occurs at 4/rev, so orders 3–5/rev were screened against the first five elastic modes; no additional crossings were identified outside this range. These results confirmed that the structural dynamic model of the medium-utility helicopter was accurately implemented and suitable for coupled aeroelastic simulations.

As a mid-fidelity reference, CAMRAD II is widely used for forward-flight rotor loads and has been cross-checked in numerous experimental and computational studies. We therefore adopt CAMRAD II as a baseline comparator for blade-level quantities (tip responses, internal forces), while separately using flight test accelerations (Appendix A) to assess rotor-to-airframe transmission. To ensure a fair comparison, the CAMRAD II model uses the same rotor planform, mass and stiffness distributions, airfoil tables as the coupled NVLM–GEBT analysis. Lifting-line aerodynamics with a free-wake inflow model were employed; CAMRAD II used a 15° azimuthal step, eight geometrically exact (nonlinear) beam elements along the blade, and a 21-panel free-wake discretization. This setup makes CAMRAD II an appropriate mid-fidelity criterion for blade-level responses, while the separate comparison to flight data (Appendix A) anchors the overall workflow to measurement.

4.1 δ-Airload Trim Analysis

An aeroelastic analysis was performed on the rotor blade of a medium-utility helicopter during forward flight. Forward flight speeds of 40, 100, and 140 knots were considered, corresponding to the low-, medium-, and high-speed conditions, respectively. For each flight condition, the target thrust was selected based on the operating weight (OPW), and trim analysis was conducted to ensure that the hub moments were minimized to approximately zero.

For each speed, the shaft tilt angle was taken from a CAMRAD II full-airframe trim and then kept fixed in the present rotor-only NVLM–GEBT calculations so that the inflow-angle effect is represented without performing a full-airframe trim within our framework.

We employed a nested coupling strategy with three time scales. The aerodynamic solver advanced with a fixed azimuth step of 5° (72 stations per revolution) and marched the free wake over five rotor revolutions to obtain a periodically converged airload field for the current blade deformation and controls. The structural solver then performed a rotor-trim calculation over 100 revolutions, applying the δ-airload correction (the difference between the external NVLM load and the internal lifting-line load from the previous pass) to the sectional forces and moments while updating control angle. This inner pair of "aerodynamics → structure" computations defines one coupled iteration. The outer coupled iteration was repeated up to eight passes; at each pass the updated controls and deformation were supplied to the aerodynamic module, and the process was considered converged when the mean absolute change of the three primary control angles between successive iterations was $\leq 0.05°$.

Table 1 Medium-utility helicopter rotor simulation conditions

Property	Value
Rotor radius [m]	7.9
Number of blade [-]	4
Tip Mach number [-]	0.661
Forward speed [knots]	40, 100, 140
Advance ratio (μ) [-]	0.09, 0.23, 0.32
Time step [°]	5
Total revolution for aerodynamic model [-]	5
Total revolution for trim analysis	100
Coupling iteration [-]	8

The detailed model specifications and analysis conditions are listed in Table 1.

Figure 6a shows the evolution of the aerodynamic loads obtained from the aerodynamic module during the aero-structural coupled analysis at 40 knots. Trim analysis incorporating δ-airloads, the difference in aerodynamic loads computed by the structural and aerodynamic modules, was applied within the structural module. Eight coupling iterations were conducted for all forward speed cases. At each iteration, the structural module updated the trimmed aerodynamic load, and the δ-airloads were observed to gradually converge as the hub loads from the aerodynamic module approached the target values. Figure 6b illustrates the convergence behavior of the pitch control angles (collective, lateral cyclic, and longitudinal cyclic) during the aero-structural coupling. Each control input gradually approached a steady value through the iterative coupled analysis. As demonstrated in the Appendix A, the resulting fuselage acceleration responses closely matched the flight test data, confirming the overall consistency and accuracy of the coupled analysis.

The coupled GEBT-NVLM solver was assessed against CAMRAD II and an internal GEBT-LLT (linear inflow) model for flapwise, lagwise, and torsional (elastic twist) blade tip motions over one rotor revolution at forward-flight speeds of 40, 100, and 140 knots (Figs. 7, 8 and 9).

Figure 7a–c shows the azimuthal variations in the blade tip flapwise displacement at 40, 100, and 140 knots, respectively. The dominant 1/rev flap bending steadily increased with the advance ratio. At 40 knots, NVLM–GEBT gave a 1/rev peak-to-peak amplitude of 0.0425 m versus 0.0678 m for CAMRAD II (37.3% lower), with a phase offset of + 18.5°; GEBT–LLT was 0.0552 m (18.6% lower), with − 101.8°. At 100 knots, 1/rev peak-to-peak amplitude of NVLM–GEBT was 0.0468 m versus 0.0708 m for CAMRAD II (33.8% lower), with + 92.3°; GEBT–LLT was 0.167 m (135.7% higher), with + 31.5°. This agreement underscores the capability of the NVLM solver to capture wake dynamics and local inflow variation more accurately

Fig. 6 Convergence history of hub loads and control angles for coupling iterations at 40 knots

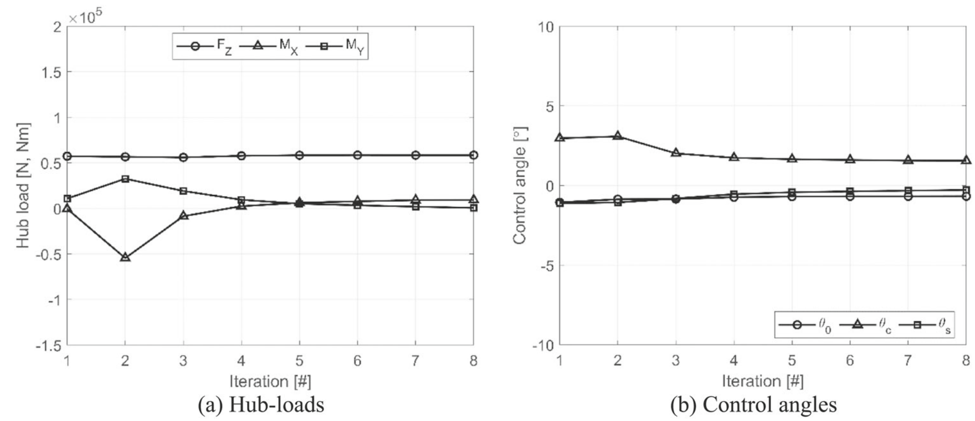

than lifting-line theory. At 140 knots, NVLM–GEBT was 0.105 m versus 0.298 m (64.7% lower), with + 97.0°; GEBT–LLT was 0.195 m (34.5% lower), with + 71.1°. While the GEBT–NVLM amplitude remained under those of CAMRAD II and GEBT–LLT, its azimuthal sectional load distribution diverged from CAMRAD II due to the development of the reverse-flow region. CAMRAD II employs a lifting-line formulation with empirically prescribed inflow models and no chordwise discretization, which limits its ability to resolve the detailed chordwise variation of aerodynamic loading [32], particularly within the reverse-flow region on the retreating side at high forward speeds. In contrast, the NVLM–VPM solver employs chordwise discretization, full-span wake modeling with both shed and trailing vortices, and a vortex particle representation of wake evolution. Moreover, separated flow effects are incorporated through sectional airfoil data and vortex strength correction, enabling more accurate prediction of aerodynamic load under high forward speed conditions. The improved ability of NVLM to capture separated flow aerodynamics and unsteady wake behavior has been validated in previous studies focusing on rotor blade separation phenomena [33]. As a result, the aeroelastic coupling produces more pronounced blade tip deformations at 140 knots.

Figure 8a–c shows the mean-removed azimuthal variation of the blade tip lagwise displacement at forward-flight speeds of 40, 100, and 140 knots, respectively. The in-plane (lag) motion, although an order of magnitude smaller than the flapwise displacement, is important for evaluating the lead–lag damping behavior.

At 40 knots, 1/rev peak-to-peak amplitude of NVLM–GEBT was 0.0185 m versus 0.0463 m for CAMRAD II (60.1% lower), with + 7.59°; GEBT–LLT was 0.0266 m (42.6% lower), with − 3.05°. CAMRAD II predicted the largest lagwise tip displacement, which is likely attributed to limitations in its lifting-line-based free-wake model, lacking the ability to accurately model in-plane vortex shedding and hub damping effects. In comparison, the coupled GEBT-NVLM solver yielded smaller amplitude, and after convergence at iteration eight, its phase trend remained consistent with that of the internal GEBT-LLT model. At 100 knots, 1/rev peak-to-peak amplitude of NVLM–GEBT was 0.0126 m versus 0.0234 m (46.2% lower), with + 16.6°; GEBT–LLT was 0.0160 m (31.7% lower), with − 19.9°. Although the GEBT-LLT model employs a linear inflow assumption and is not an aerodynamic high-fidelity reference, its amplitude and phase trends still provide a useful baseline for internal consistency checks of the structural response. At 140 knots, 1/rev peak-to-peak amplitude of NVLM–GEBT was 0.0105 m versus 0.0158 m (34.0% lower), with − 106.4°; GEBT–LLT was 0.0121 m (23.3% lower), with − 49.1°. This residual discrepancy may have resulted from differing assumptions regarding hub damping or in-plane aerodynamic-structural coupling. The improvement from iterations one to eight highlights the importance of including structural feedback to accurately capture lagwise dynamics, even under moderate-fidelity aerodynamic modeling.

Figure 9a–c shows the azimuthal variation in the blade tip elastic twist response at forward-flight speeds of 40, 100, and 140 knots, respectively.

At 40 knots, the 1/rev peak-to-peak amplitude of NVLM–GEBT was 0.262° versus 0.318° for CAMRAD II (17.4% lower); GEBT–LLT was 0.288° (9.2% lower). The three solvers produced nearly identical waveforms and amplitudes, indicating that under low-advance-ratio conditions, the elastic contribution to torsion was limited, and differences in the modeling approaches had a minimal impact on the overall pitch behavior. At 100 knots, the 1/rev peak-to-peak amplitude of NVLM–GEBT was 0.270° versus 0.170° for CAMRAD II (58.8% higher), while GEBT–LLT was 0.196° (15.1% higher). NVLM–GEBT lies between CAMRAD II and GEBT–LLT while preserving the common sinusoidal character. At 140 knots, the 1/rev peak-to-peak amplitude of NVLM–GEBT was 0.415° versus 0.455° for

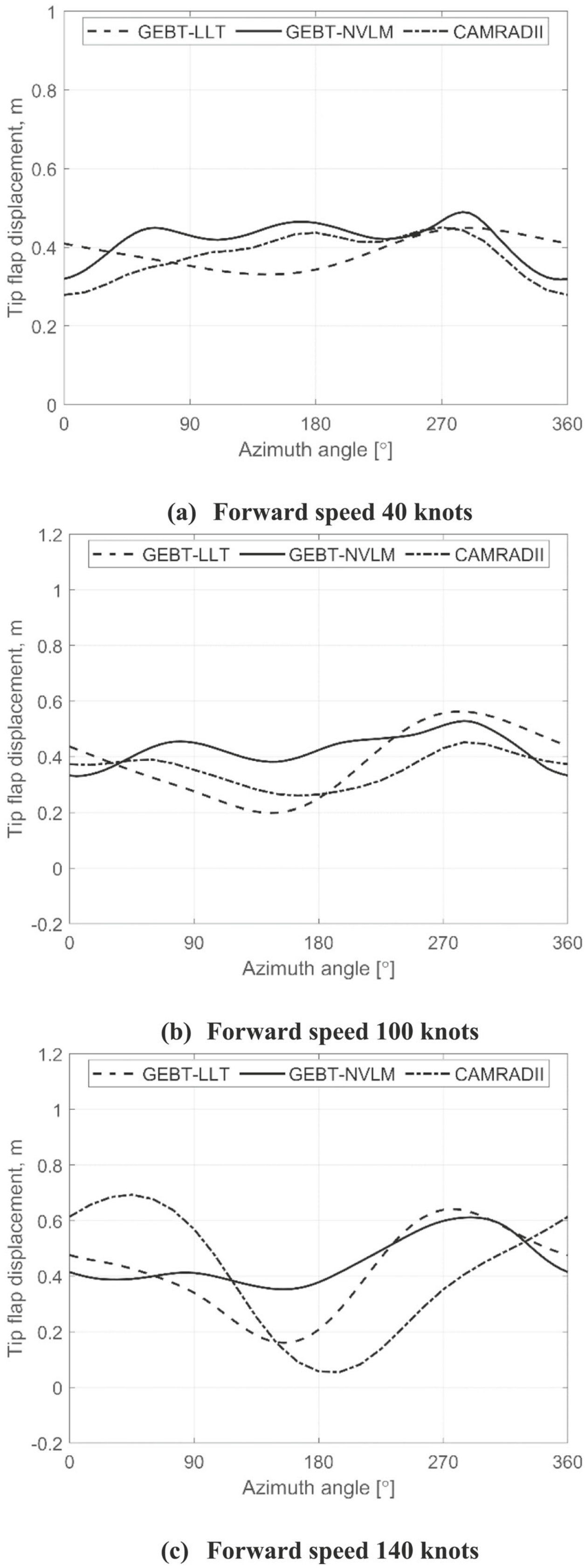

(a) Forward speed 40 knots

(b) Forward speed 100 knots

(c) Forward speed 140 knots

Fig. 7 Flapwise displacement of the blade tip at various forward-flight speeds

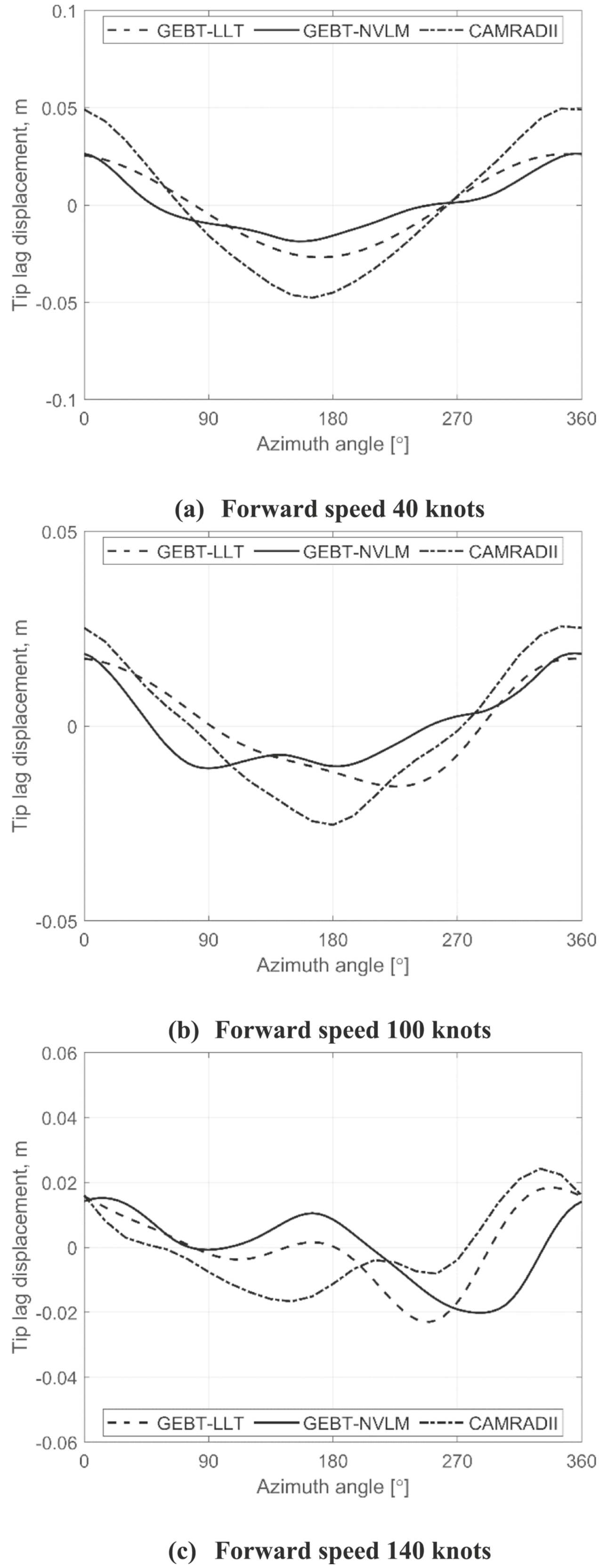

(a) Forward speed 40 knots

(b) Forward speed 100 knots

(c) Forward speed 140 knots

Fig. 8 Lagwise displacement of the blade tip at various forward-flight speeds with the mean removed

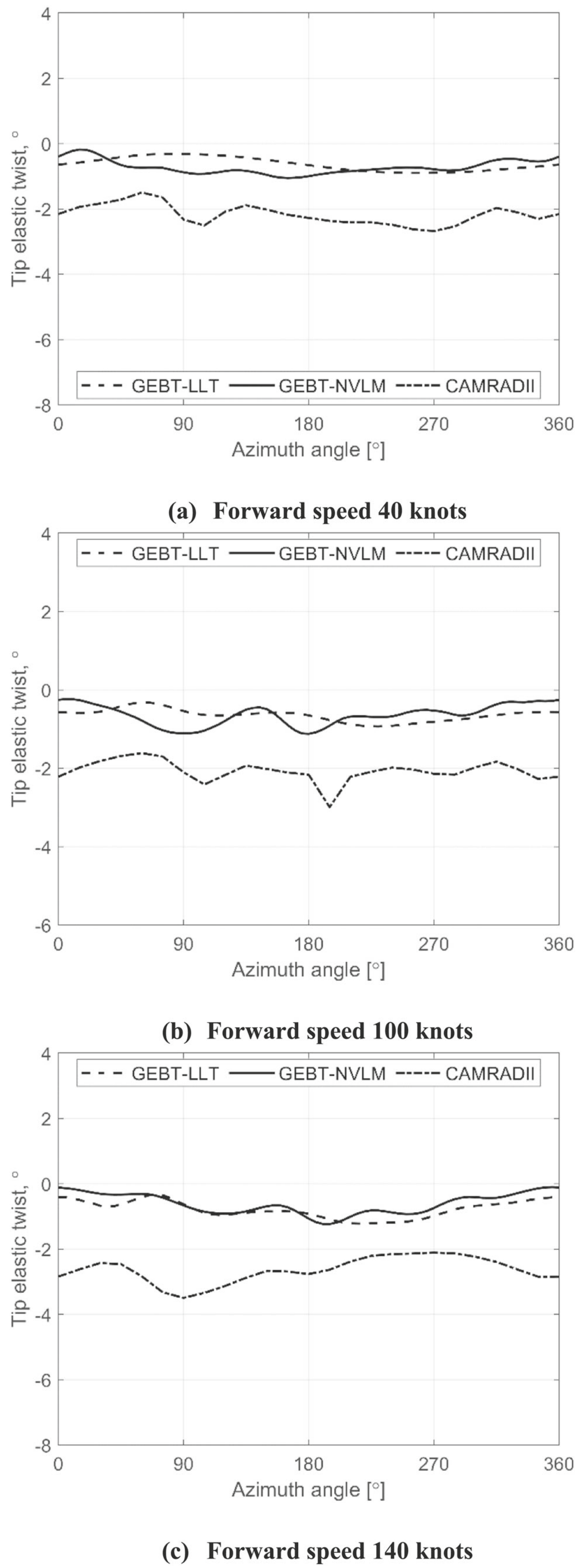

(a) **Forward speed 40 knots**

(b) **Forward speed 100 knots**

(c) **Forward speed 140 knots**

Fig. 9 Elastic twist of the blade tip at various forward-flight speeds

CAMRAD II (8.7% lower), while GEBT–LLT was 0.334° (26.6% lower).

Across speeds, NVLM–GEBT and GEBT–LLT deliver comparable amplitudes, while their phases differ by a few–tens of degrees depending on advance ratio; both retain a predominantly sinusoidal 1/rev character. Overall, the close magnitude of NVLM–GEBT and GEBT–LLT and their consistent 1/rev patterns indicate that the structural model drives a similar elastic response under both inflow formulations, whereas nearly 1.8° absolute offset relative to CAMRAD II is likely due to variations in the distinct aerodynamic inflow models and torsional stiffness representations across the methods, rather than the limitations inherent to any single approach.

Figure 10a–c summarizes the trimmed control angles, i.e., collective θ_0, lateral cyclic θ_c, and longitudinal cyclic θ_s, obtained at 40, 100, and 140 knots for the four solvers (GEBT–NVLM, GEBT–LLT, NVLM, and CAMRAD II). Across all speeds the qualitative trends are consistent: θ_0 grows with forward speed, θ_c is positive and increases with speed (roll-right requirement on the advancing side), and θ_s becomes increasingly negative (aft cyclic to balance retreating-side lift loss). The two GEBT-based solvers yield closely clustered controls at each condition, indicating that the structural model dictates a similar elastic response regardless of whether the inflow is resolved by NVLM or approximated by LLT. Differences between the GEBT-based results and CAMRAD II/NVLM reflect how each aerodynamic model distributes inflow and wake curvature; these differences are most visible in θ_0 and θ_s at 140 knots, whereas the overall ordering and sign of θ_c and θ_s remain the same for all solver. Taken together, the figure shows that the characteristic control trends are preserved by the coupled framework, and that NVLM-specific wake features propagate through the loose coupling into trim while still producing control angles that are consistent in magnitude and direction with the other references.

Figure 11a–c shows the mean-removed flap bending moment at the 0.17 R station for forward-flight speeds of 40, 100, and 140 knots, comparing the coupled GEBT–NVLM prediction with CAMRAD II. The response was dominated by the 3/rev component across all speeds. At 40 knots, the 3/rev peak-to-peak amplitude was 754.6 Nm for NVLM–GEBT versus 157.7 Nm for CAMRAD II (378.5% higher), with a 3/rev phase offset of + 62.8°. At 100 knots, the 3/rev peak-to-peak amplitude was 650.6 Nm for NVLM–GEBT versus 174.4 Nm for CAMRAD II (273.0% higher), with a 3/rev phase offset of − 13.9°. At 140 knots, the 1/rev peak-to-peak amplitude was 362.0 Nm for NVLM–GEBT versus 388.6 Nm for CAMRAD II (6.8% lower), and the 3/rev peak-to-peak amplitude was 625.5 Nm versus 229.1 Nm (173.0% higher).

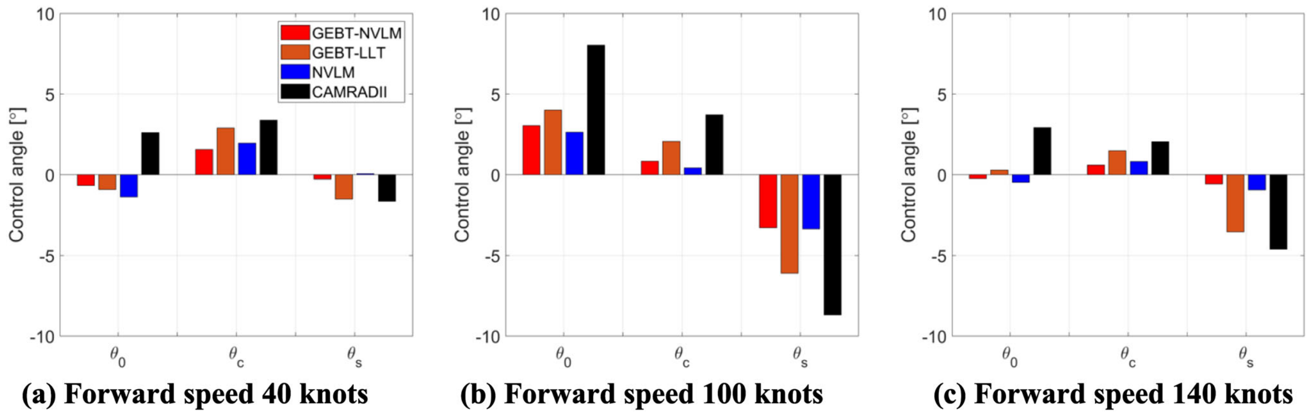

Fig. 10 Trimmed control angles at various forward-flight speeds

Overall, the coupled solver maintained correct phasing across all advance ratios while systematically delivering larger bending amplitudes, underscoring the influence of the higher fidelity wake representation on the root-bending loads.

Figure 12a–c illustrates the mean-removed azimuthal variations in the torsional (pitching) moment at the 0.17 R span station for forward-flight speeds of 40, 100, and 140 knots, respectively. At 40 knots, the 1/rev peak-to-peak amplitude was 98.8 Nm for NVLM–GEBT versus 121.4 Nm for CAMRAD II (18.6% lower), with a 1/rev phase offset of + 71.8°. At 100 knots, the 1/rev peak-to-peak amplitude was 168.0 Nm for NVLM–GEBT versus 95.7 Nm for CAMRAD II (75.6% higher), with a 1/rev phase offset of + 48.5°. At 140 knots, the 1/rev peak-to-peak amplitude was 287.1 Nm for NVLM–GEBT versus 233.1 Nm for CAMRAD II (23.2% higher), with a 1/rev phase offset of – 0.49°.

Across all speeds, the coupled solver reproduced the dominant 1/rev character and phase of the reference solution while delivering amplitude variations that remained within engineering tolerance, indicating that the mixed-variational GEBT formulation and NVLM wake captured the essential elastic-twist dynamics of the blade root region.

Figure 13a–c shows the mean-removed azimuthal variation in the lag-bending moment at the 0.17 R span for forward-flight speeds of 40, 100, and 140 knots, respectively. Both 1/rev and 3/rev components are significant. At 40 knots, the 1/rev peak-to-peak amplitude was 275.6 Nm for NVLM–GEBT versus 636.2 Nm for CAMRAD II (56.7% lower), with a 1/rev phase offset of + 21.9°; the 3/rev peak-to-peak amplitude was 409.8 Nm versus 454.9 Nm (9.9% lower), with a 3/rev phase offset of – 12.9°, indicating that both solvers captured the principal timing of the in-plane loading, whereas the NVLM wake yielded a slightly lower amplitude. At 100 knots, the 1/rev peak-to-peak amplitude was 209.8 Nm for NVLM–GEBT versus 369.7 Nm for CAMRAD II (43.3% lower), with a 1/rev phase offset of + 63.5°; the 3/rev peak-to-peak amplitude was 230.3 Nm versus 346.1 Nm (33.5% lower), with a 3/rev phase offset of – 79.1°. At 140 knots, the 1/rev peak-to-peak amplitude was 505.0 Nm for NVLM–GEBT versus 854.4 Nm for CAMRAD II (40.9% lower), with a 1/rev phase offset of + 65.9°; the 3/rev peak-to-peak amplitude was 162.2 Nm versus 725.9 Nm (77.7% lower), with a 3/rev phase offset of – 156.4°.

Across all three speeds, the coupled solver tracked the major azimuthal features of the reference solution, whereas its lower amplitude reflected the different inflow and structural damping representations used by the two solvers. The results confirm that the mixed-variational GEBT model together with the NVLM wake can reproduce the essential lag-bending dynamics over a wide advance ratio range.

For clarity, Sect. 4.1 concludes with a concise summary that synthesizes the harmonic metrics (1P/3P peak-to-peak and 1P/3P phase offsets) into the comparative strengths and limitations of each solver. Across 40–140 knots, the coupled NVLM–GEBT reproduces the dominant 1/rev (and, where present, 3/rev) content and phase trends, while showing speed-dependent amplitude differences attributable to inflow representation and torsional/lead–lag coupling. CAMRAD II offers a mature lifting-line/free-wake reference; its amplitudes are sensitive to inflow/wake settings and azimuthal step, but it provides a consistent phase reference for comparison. The internal GEBT–LLT is not an aerodynamic high-fidelity model; however, it serves as a structural-consistency baseline under linear inflow, helping to isolate structural effects from wake modeling.

4.2 Aerodynamic Load and Wake Structure

Before presenting the rotor aerodynamic load distributions in forward flight, the aerodynamic module was validated against the HART II experimental database. Figure 14 compares the sectional normal force coefficient at 87% blade span with experimental data and previously published results. The present NVLM predictions reproduce the main experimental

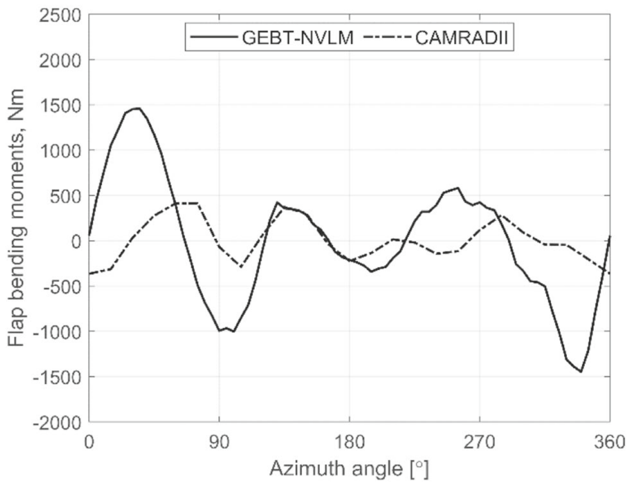

(a) Forward speed 40 knots

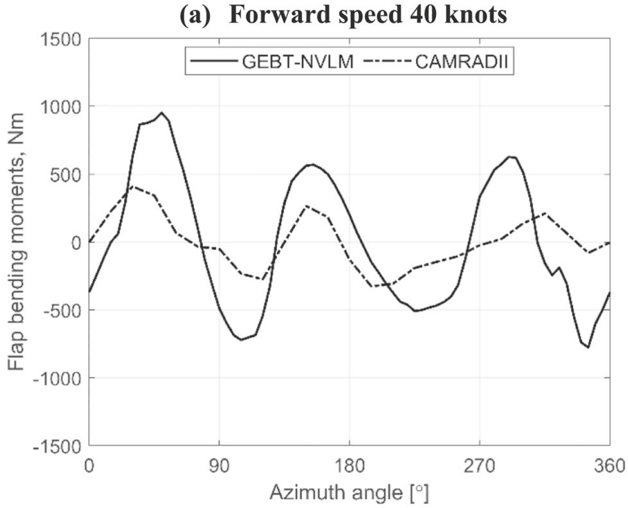

(b) Forward speed 100 knots

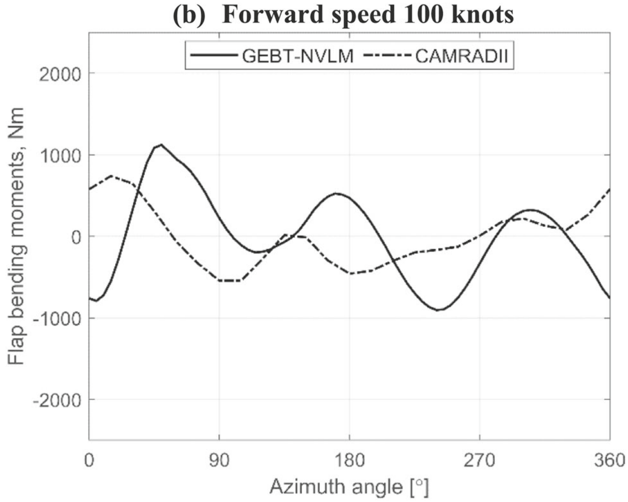

(c) Forward speed 140 knots

Fig. 11 Flap bending moments at 0.17 R with the mean removed

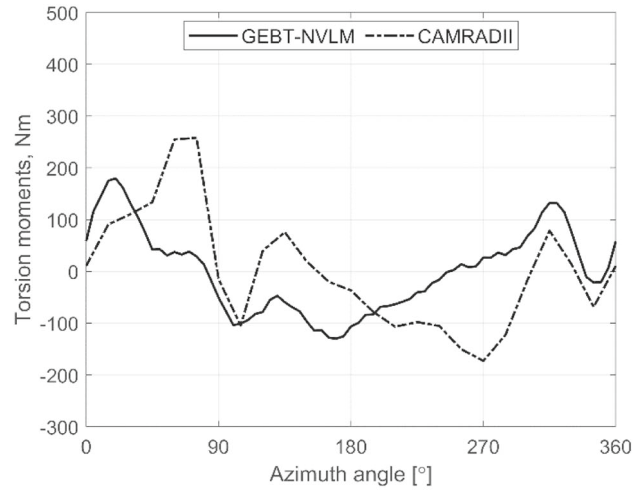

(a) Forward speed 40 knots

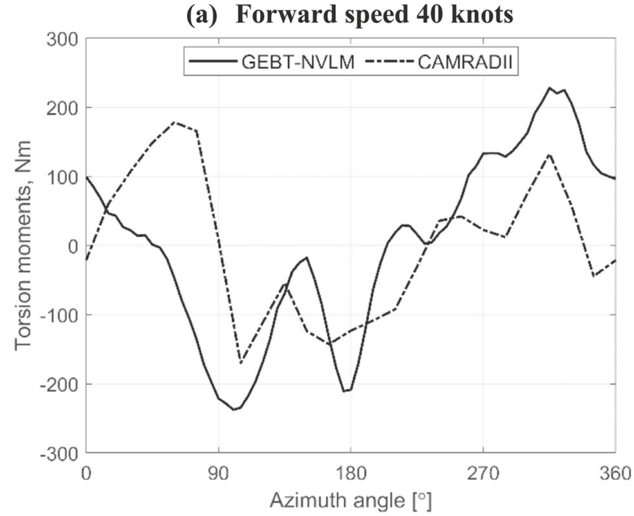

(b) Forward speed 100 knots

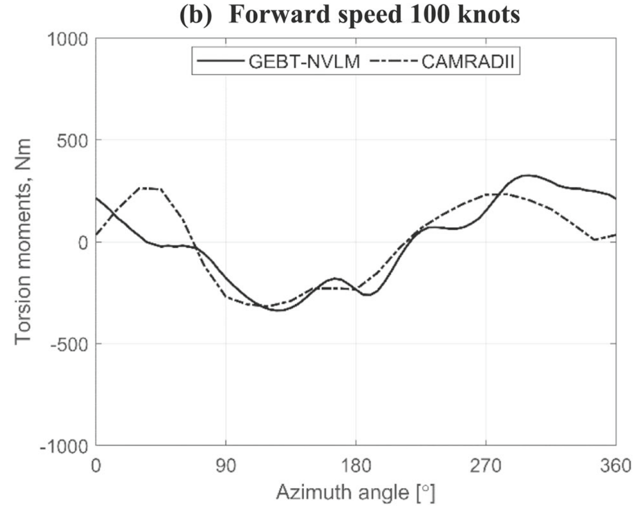

(c) Forward speed 140 knots

Fig. 12 Torsion moments at 0.17 R with the mean removed

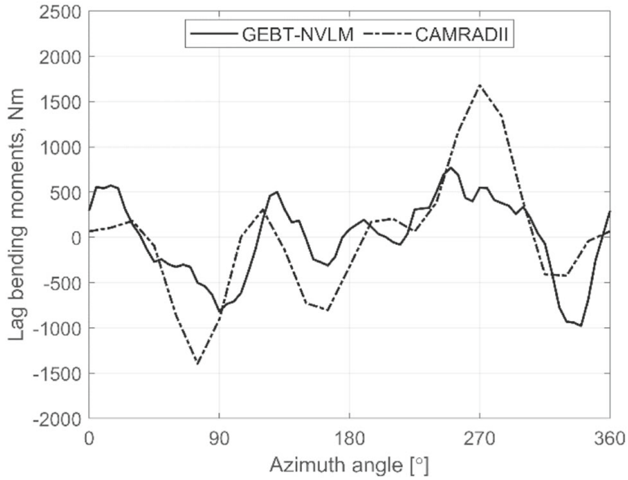

(a) Forward speed 40 knots

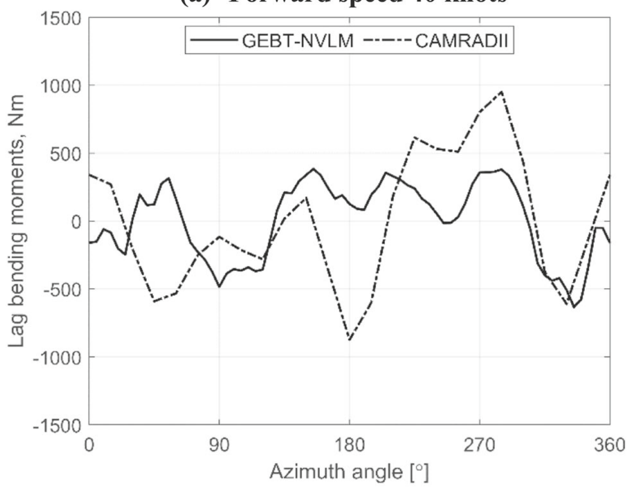

(b) Forward speed 100 knots

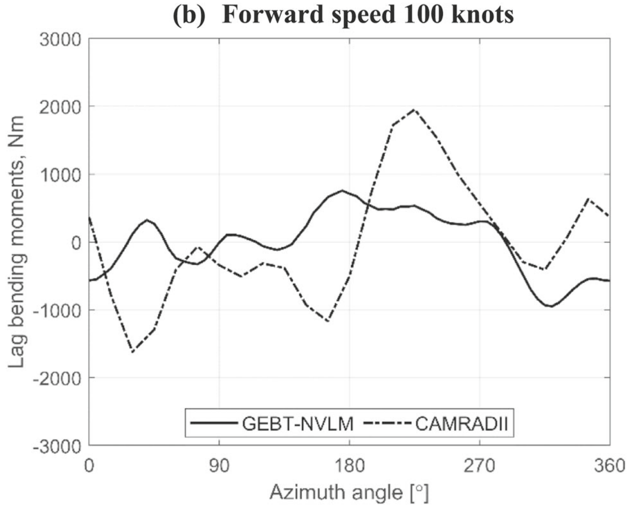

(c) Forward speed 140 knots

Fig. 13 Lag bending moments at 0.17 R with the mean removed

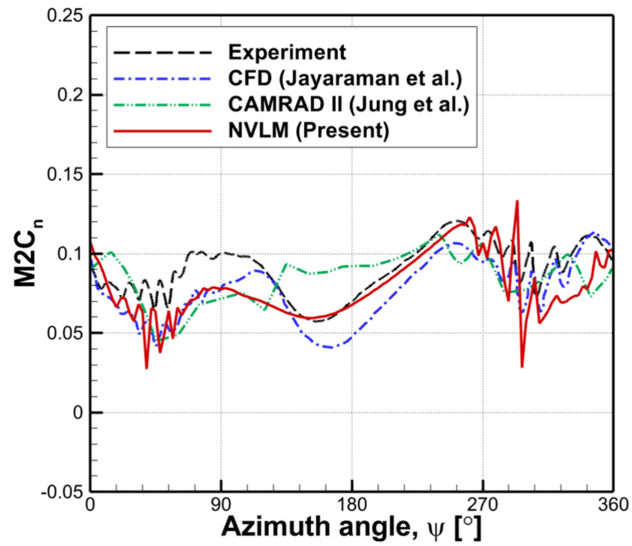

Fig. 14 Comparison of time history of normal force distribution at $r/R = 0.87$

features: the normal force around 90° is slightly underpredicted, the load reduction near 170° is well captured, and the onset of blade–vortex interaction between 270° and 360° is predicted at the correct azimuth. Although the BVI peak amplitude tends to be overestimated due to limited numerical dissipation in the VPM, the NVLM results agree more closely with the experimental measurements than CAMRAD II and are comparable to CFD-based predictions. This validates the accuracy of the present solver and demonstrates its capability to predict unsteady aerodynamic characteristics for rotor aeroelastic analysis. Figures 15 and 16 compare the sectional normal force distributions of the main rotor blade in forward flight for rigid and flexible-blade configurations, respectively. These contour maps provide a comprehensive azimuthal-spatial visualization of the unsteady aerodynamic loading over one rotor revolution at three advancing flight speeds: 40, 100, and 140 knots.

In the rigid-blade case (see Fig. 15), the aerodynamic loads exhibit highly asymmetric patterns across the rotor disc. At 40 knots, a pronounced crescent-shaped high-loading region appears on the advancing side (around the azimuth angle of 90°), due primarily to the forward shaft tilt enhancing the effective angle of attack. The loading distribution is more symmetric along the span but clearly biased azimuthally. At 100 knots, a reverse-flow region becomes evident on the retreating side near the azimuth angle of 270°, where chordwise inflow becomes negative, inducing local stall phenomena. This stall region is characterized by strong adverse pressure gradients and is known to exacerbate vibratory loads. A secondary loading concentration also appears near the azimuth angle of 330°, where the local inflow aligns with blade motion. At 140 knots, the reverse-flow region

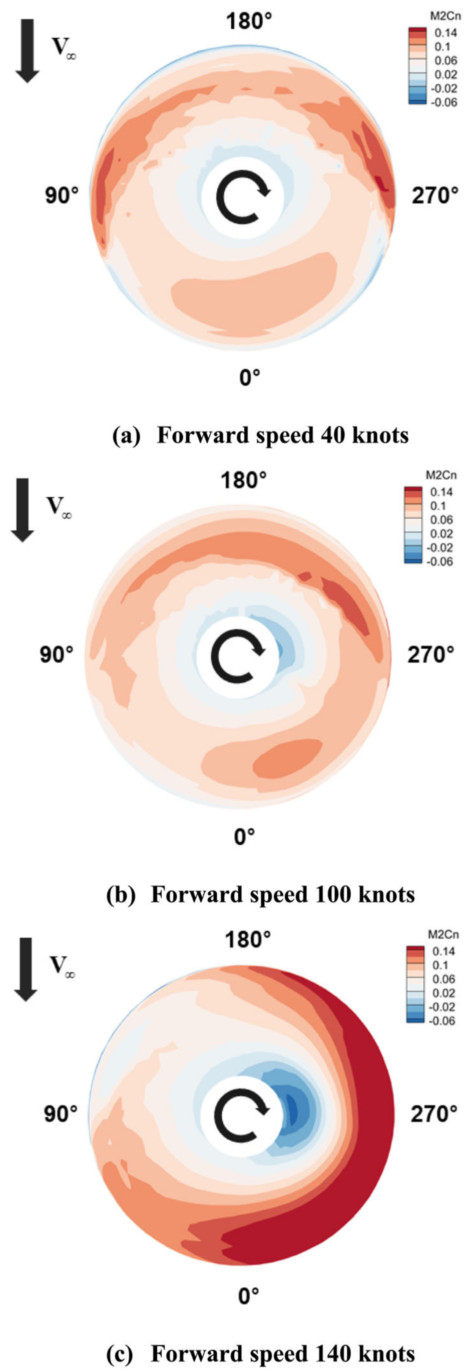

Fig. 15 Sectional normal force distributions of the rigid rotor blade at different forward-flight speeds

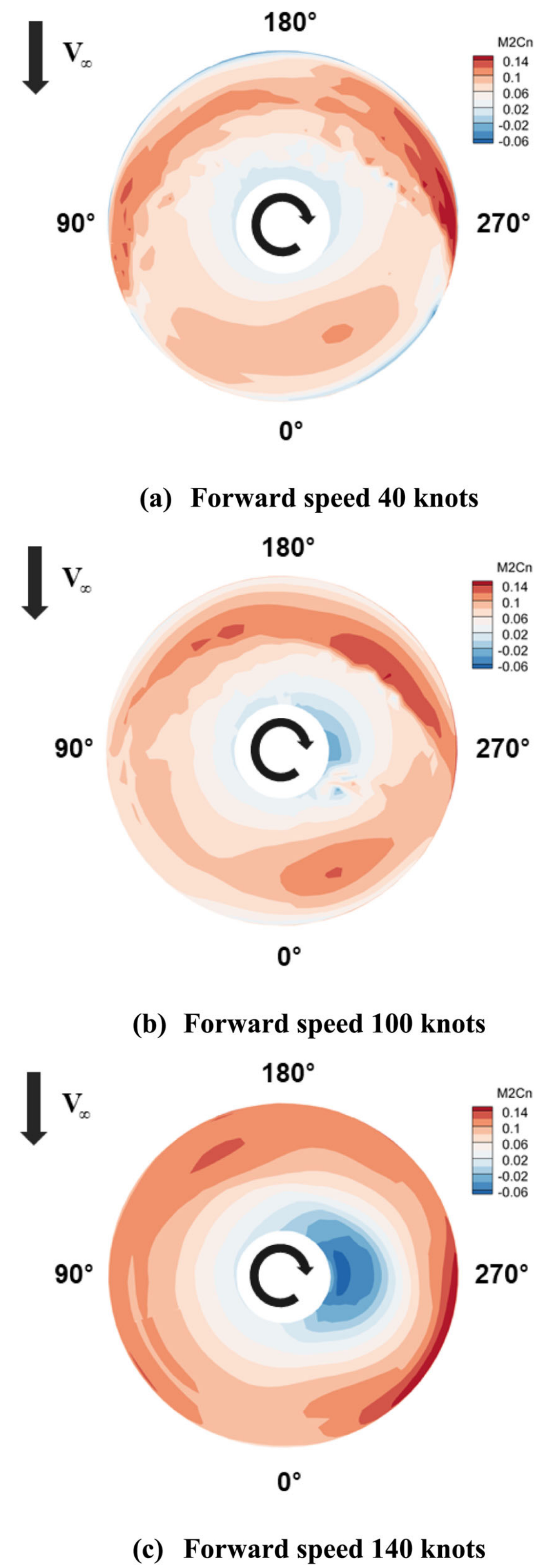

Fig. 16 Sectional normal force distributions of the deformed rotor blade at different forward-flight speeds

further expands, covering a larger azimuthal range due to the increased advance ratio. Peak loads are intensified and remain concentrated on the retreating side, following a similar crescent pattern. In contrast, the flexible-blade results (see Fig. 16) show notable differences in both load magnitude and spatial distribution. At 40 knots, the consideration of structural flexibility increases the maximum normal force, especially in the advancing-side region, due to elastic amplification of angle of attack. However, the load contours appear more diffused spanwise, implying smoother aerodynamic response. At 100 knots, although the reverse-flow region still forms near the azimuth angle of 270°, its intensity is reduced, and the load peak at the azimuth angle of 330° is mitigated. The structural deformation attenuates the amplitude of dynamic loads and promotes a more uniform distribution across the azimuth angle. At 140 knots, this effect becomes more pronounced, with the peak loading regions shifting toward the azimuth angles of 180° and 330°. Compared to the rigid-blade case, the overall load amplitude is reduced, and the azimuthal distribution becomes more diffused, reflecting increased damping and phase lag associated with the elastic response of the rotor blade. Flapping displacement alters the effective velocity components experienced by each blade section, thereby modifying the effective angle of attack. This induces changes in aerodynamic loads, which in turn drive further structural responses through aeroelastic feedback. Consequently, since the flapping displacement is the largest at 140 kts, the differences between the rigid and flexible-blade sectional normal force contours become most significant. This observation is consistent with the earlier aerodynamic findings, where the reverse-flow region and stronger unsteady wake interactions at high speed led to enhanced blade deformation.

The wake structure of helicopter rotors plays a critical role in determining the unsteady aerodynamic environment, vibratory loads, and potential BVI phenomena. In this study, the rotor wake was modeled using the Lagrangian-based VPM, which allows for accurate and grid-free resolution of complex vortex dynamics including tip-vortex roll-up, self-induction, and convection under varying flight conditions. VPM captures the continuous evolution of vortex particles shed from the blade tips and trailing edges, offering insight into the interaction between wake structure and rotor blades. Figures 17 and 18 present the predicted wake structures of the deformed rotor blade at forward-flight speeds of 40, 100, and 140 knots. Figure 17 provides a side view in the x–z plane, while Fig. 18 offers an isometric perspective to illustrate the three-dimensional characteristics of the wake evolution. As the forward speed increases, a larger shaft tilt angle is employed to produce the required propulsive force, resulting in enhanced aerodynamic asymmetry across the rotor disc. This asymmetry significantly alters the wake geometry and tip-vortex trajectories. At 40 knots, the wake exhibits a moderately contracted helical pattern with relatively short axial pitch. The tip vortices remain close to the rotor plane, indicating slower convection and stronger potential for self-induced interactions. As the speed increases to 100 knots, the wake becomes more elongated along the downstream direction. The axial spacing of the tip vortices increases, and their overall structure becomes more stretched and orderly due

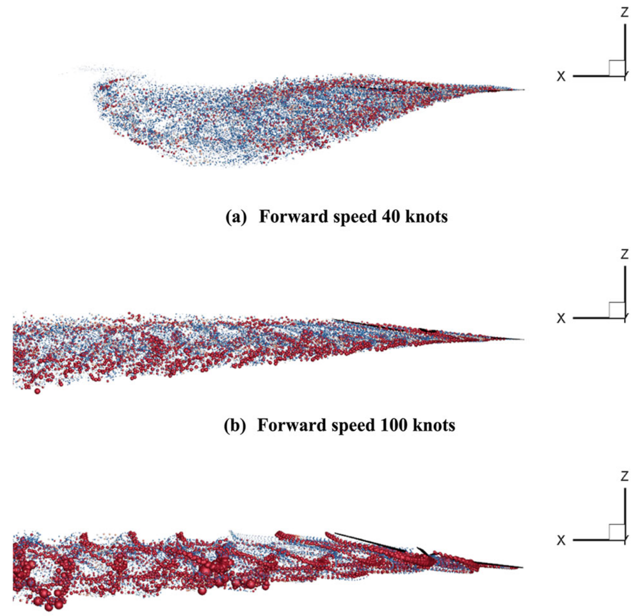

(a) Forward speed 40 knots

(b) Forward speed 100 knots

(c) Forward speed 140 knots

Fig. 17 Wake structures in the x–z plane at different forward-flight speeds

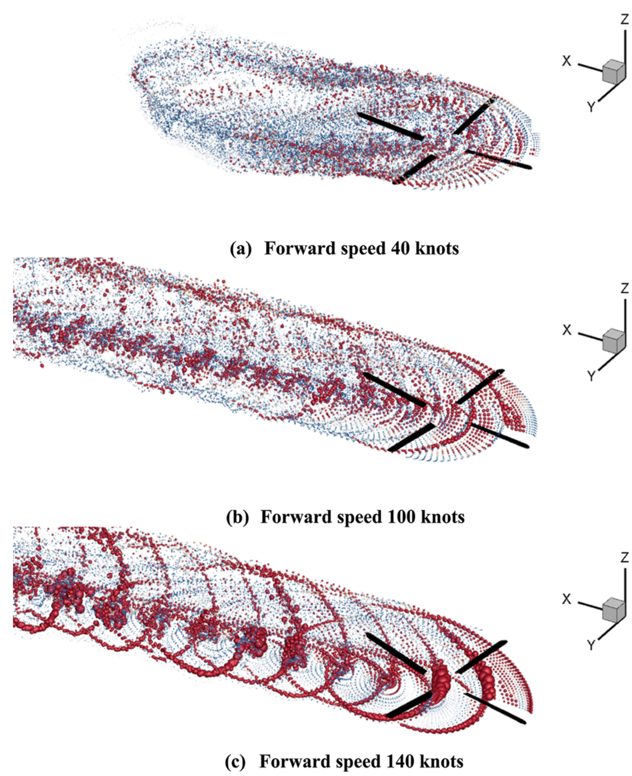

(a) Forward speed 40 knots

(b) Forward speed 100 knots

(c) Forward speed 140 knots

Fig. 18 Isometric view of wake structures at different forward-flight speeds to higher free-stream velocity. At 140 knots, the most distinct wake features are observed: the tip vortices display the longest axial pitch distance, and the wake sheet is convected far downstream with minimal curvature. This is primarily attributed to the combination of a large shaft tilt and high advance ratio, which promotes faster downstream convection and reduces wake recirculation near the rotor plane. A notable contrast in vortex strength is also observed between the advancing side and retreating sides, especially at higher speeds. The asymmetry becomes more pronounced as the rotor operates under stronger inflow gradients. In both the 100- and 140-knot cases, the wake convects rapidly away from the rotor, and no evidence of BVI is found in the near-wake region. This observation is consistent with the loading distributions discussed previously and confirms that, at high forward speeds, the rapid downstream convection of the wake inhibits blade–vortex interaction by maintaining sufficient spatial separation between the blades and their own shed vortices.

5 Conclusions

This study developed a modular, mid-fidelity GEBT–NVLM aeroelastic framework that couples a surface-resolved lifting-surface aerodynamic solver to a mixed-variational GEBT structural model through a δ-airload loose-coupling procedure. The method achieved trimmed forward-flight solutions at advance ratios 0.09–0.32 (40, 100, 140 knots) with robust convergence in eight coupled iterations.

Validation in this work follows two tiers. First, a code-to-code check against CAMRAD II quantifies agreement using harmonic metrics, i.e., 1/rev (and, where relevant, 3/rev) peak-to-peak amplitudes and 1/rev phase offsets, for blade tip kinematics and root-bending/torsional moments. Across speeds, the coupled solver reproduces the dominant harmonic content and phase trends, while revealing speed-dependent amplitude differences attributable to inflow representation and torsional/lead–lag coupling. Second, a flight test-to-model check is provided in Appendix A, where predicted fuselage accelerations at four instrumentation stations are compared with flight test spectra to demonstrate system-level consistency. From a practical standpoint, the framework offers (i) physics-resolved wake/airload prediction without the prohibitive cost of tight CFD/CSD coupling, (ii) a mixed-variational formulation based geometrically exact beam that preserves inertial and geometric nonlinearities, and (iii) transparent sub-model interfaces suitable for sensitivity studies and early-stage active control evaluation.

Current limitations include the absence of blade-thickness and dynamic-stall effects in the lifting-surface model, and the lack of a same-condition CFD/CSD cross-benchmark within this paper. Future work will integrate HHC and IBC modules for active vibration reduction and perform parametric trade-off analyses. Moreover, a comparative study using high-fidelity CFD/CSD coupling will be conducted to quantify the accuracy and computational advantages of the mid-fidelity framework across a broader range of flight regimes.

Appendix A: Numerical Results of Rotor-Fuselage Coupled Analysis

A.1 One-Way Coupled Analysis

A dynamic response prediction framework was assembled in NX NASTRAN by combining a 3D FE fuselage model (Fig. 19) with rotor/fuselage one-way coupling. The baseline model used solid elements for all primary structures to retain realistic mass and stiffness distributions, and included both overall structural damping and mode-specific damping, consistent with the verification setup. A ground-vibration-test configuration was obtained by suspending the airframe with bungee cables modeled as linear beam elements. The cable mass was neglected, and its elastic modulus, cross-sectional area, and length were chosen such that: (i) the rigid-body natural frequencies remained < 1 Hz, and (ii) the first few elastic-mode frequencies matched the full-airframe results within engineering tolerance.

See Fig. 19.

Rotor hub forces and moments, obtained from the converged aero-structural trim solution, were applied at the mast-interface grid through rigid-body element constraints, ensuring consistent transfer of the six-component dynamic

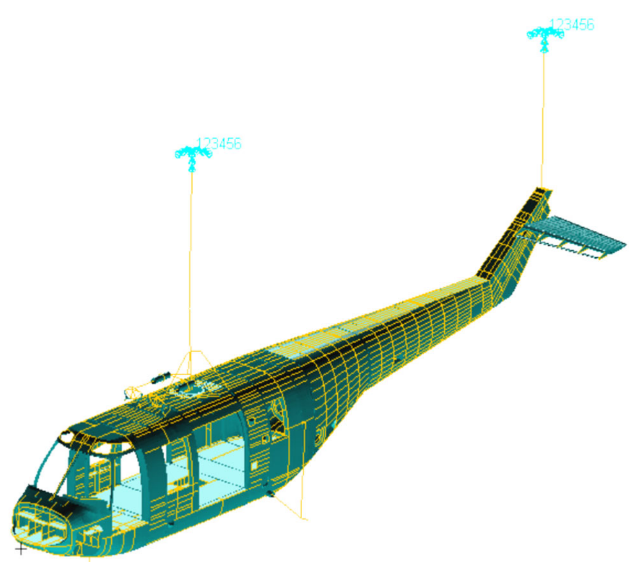

Fig. 19 FE model of a platform aircraft fuselage

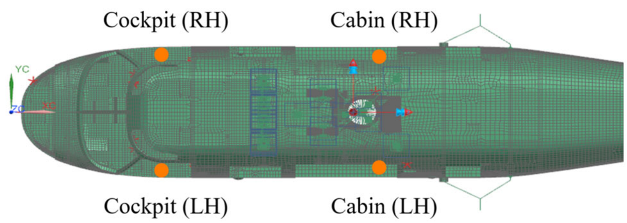

Fig. 20 Locations of fuselage acceleration sensors

load vector to the fuselage. The dynamic response was solved using a modal frequency–response procedure. First, normal-mode analysis yielded eigenvalues and mode shapes within the frequency range of 4 /rev excitation. Steady-state acceleration responses were recovered at four flight test sensor locations: cockpit-LH, cockpit-RH, cabin-LH, and cabin-RH (left-hand: LH; right-hand RH). These numerical results were later compared with the measured spectra to validate the coupled aero-structure–fuselage framework.

A.2 Validation of Vibrations at the Cockpit and Cabin

The acceleration responses at key cockpit and cabin sensor locations were obtained for each forward-flight condition. Figure 20 shows the four accelerometer positions used in both the numerical model and flight test: cockpit-LH and cockpit-RH stations near the pilot seats and cabin-LH and cabin-RH stations aft of the mast.

See Fig. 20.

Figure 21 compares the steady-state vertical accelerations predicted by the simulation with the flight test data at 40, 100, and 140 knots. White diamonds show the measured mean values, red bars show the numerical predictions, and thin blue horizontal lines denote the ± 30% tolerance band specified in the certification guideline; every prediction fell within this band. The solver also reproduced the relative ranking of the four locations; cockpit responses dominated at 40 knots, whereas cabin responses grew more rapidly with speed and surpassed cockpit levels by 140 knots, indicating that the overall vibration pattern was well captured.

See Fig. 21.

Table 2 lists the relative errors. Most locations were within 10%–30% of the measurements; the cockpit-LH sensor at 100 knots showed the largest deviation (27.3%), while the cabin-RH sensor at 140 knots showed the smallest (3.3%). No systematic bias toward over- or under-prediction was observed, suggesting that the structural model and damping specification are adequate for this maneuver.

See Table 2.

The strong agreement at all four stations demonstrated that the full-order fuselage model, excited solely by the rotor hub loads produced by the coupled GEBT-NVLM solver, could replicate the measured vibration environment within the accepted ± 30% envelope. As no additional tuning forces were introduced, this correlation indicated that the magnitude and phasing of the hub loads were generated with sufficient fidelity. The remaining discrepancies, most noticeable at cockpit-LH, were attributed to local equipment and attachment details that were simplified in the FE mesh, rather than to limitations in the hub-load prediction itself. Accordingly, the results confirmed that the proposed coupling framework

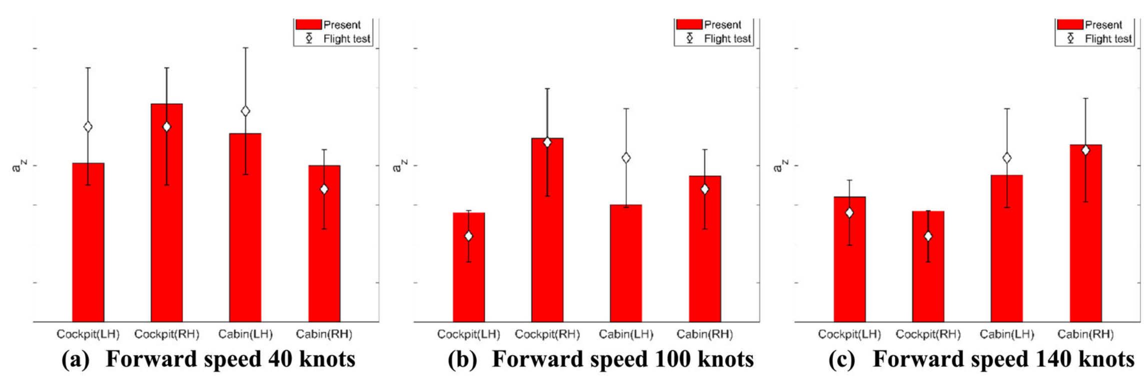

Fig. 21 Comparison of predicted and measured fuselage accelerations at different forward-flight speeds

Table 2 Relative errors of acceleration responses compared to flight test data at sensor locations for each flight speed

Flight speed [knots]	Relative error [%]			
	Cockpit (LH)	Cockpit (RH)	Cabin (LH)	Cabin (RH)
40	18.8	11.6	10.9	19.6
100	27.3	2.4	28.3	9.7
140	14.2	28.7	10.4	3.3

provides rotor hub forces and moments of realistic quality, and is suitable for subsequent studies on vibration reduction and active control strategies.

Acknowledgements This work was supported by a Korea Institute of Energy Technology Evaluation and Planning (KETEP) grant funded by the Korea government (MOTIE) (20224000000220, Jeonbuk Regional Energy Cluster Training of human resources).

Funding MOTIE, 20224000000220.

Data availability The datasets generated and/or analyzed during the current study are not publicly available due to confidentiality agreements with the helicopter manufacturer.

Declarations

Conflict of interest The authors declare that there is no conflict of interest regarding the publication of this paper.

References

1. Choi GM (2011) Helicopter vibration phenomenon. Def Technol 387:84–95
2. Kessler C (2010) Active rotor control for helicopters: motivation and survey on higher harmonic control. In: Proceedings of the 36th European rotorcraft forum, Paris, France
3. Wang S, Cheng Q (2022) Cfd-csd method for rotor aeroelastic analysis with free-wake model. Aircr Eng Aerosp Technol 95(1):132–144
4. Huang Q, Abdelmoula A, Chourdakis G, Rauleder J, and Uekermann B (2021) CFD/CSD coupling for an isolated rotor using preCICE. In: Proceedings of the 14th world congress on computational mechanics (WCCM-XIV), Online
5. Wang S, Han J, Yun H, Chen X (2021) CFD-CSD method for coupled rotor-fuselage vibration analysis with a free-wake / panel coupled model. Proc Inst Mech Eng Part G J Aerosp Eng 235(11):1343–1354
6. Fleischmann D Weber S and Lone MM (2018) Fast computational aeroelastic analysis of helicopter rotor blades, AIAA-2018–1044, AIAA aerospace sciences meeting, Kissimmee, FL
7. Kang HJ, Kim DH, Wie SY (2014) Aerodynamic and noise calculations of helicopter rotor blades using loose CFD-CSD coupling methodology. J Comput Fluids Eng 19(3):62–68
8. Yoon SH, Cho H, Shin SJ, Huh S, Koo J, Ryu J, Kim C (2021) Effect of leading-edge and vein elasticity on aerodynamic performance of flapping-wing micro air vehicles. J Korean Soc Aeronaut Space Sci 49(3):185–195
9. Jeong I, Cho H, Kang SH, and Kim H (2024) Feasible model-order reduction approach for analysis of composite rotor blades based on a geometrically exact beam formulation. Aerospac Sci Technol, 109312
10. Palaia G, Abu Salem K, Cipolla V, Binante V, Zanetti D (2021) A conceptual design methodology for e-VTOL aircraft for urban air mobility. Appl Sci 11(22):10815
11. Park J (2024) Simultaneous vibration reduction and performance improvement of helicopter rotor using individual blade pitch control with multiple harmonic inputs. Int J Aeronaut Space Sci 25:1330–1342
12. Chen J, Liu Y, Chen X, Tang L, Xiong Z (2025) Dynamic take-off and landing control for multi-rotor eVTOL aircraft. Int J Aeronaut Space Sci 26:376–389
13. Bhalla S, Kim D, Choi D (2025) Enhancing human comfort in eVTOL aircraft assisted by control moment gyroscopes. Int J Aeronaut Space Sci 26:698–718
14. Wernicke RK, and Drees JM (1963) Second harmonic control. In: Proceedings of the American helicopter society 19th annual forum, Washington, D.C.
15. Splettstößer WR, Kube R, Seelhorst U, Wagner W, Boutier A, Micheli F, Mercker E, and Pengel K (1995) Higher harmonic control aeroacoustic test (HART)—test documentation and representative results, DLR Report IB 129–95/28
16. Splettstößer WR, Kube R, Seelhorst U, Wagner W, Boutier A, Micheli F, Mercker E, and Pengel K (1989) Key results from a higher harmonic control aeroacoustic rotor test (HART) in the German-Dutch wind tunnel. In: Proceedings of the 21st European rotorcraft forum, Saint-Petersburg, Russia, 30 Aug–1 Sep
17. Bang S, Park J, Kim D, Kang U (2023) Vibration reduction simulations of a medium-utility helicopter rotor using higher-harmonic pitch control. J Korean Soc Aeronaut Space Sci 51(5):345–353
18. Hong S, You Y, Jung SN, Kim DH (2019) Vibratory loads reduction of a coaxial rotorcraft using an individual blade control scheme. J Korean Soc Aeronaut Space Sci 47(5):364–370
19. Lim JW, Tung C, Yu YH (2001) Prediction of blade-vortex interaction airloads with higher-harmonic pitch control using the 2GCHAS comprehensive code. J Press Vessel Technol 123(4):469–474
20. Johnson W (1994) Technology drivers in the development of CAMRAD II. In: Proceedings of the AHS aeromechanics specialists' conference, San Francisco, CA
21. Bauchau OA, Bottasso CL, Nikishkov YG (2001) Modeling rotorcraft dynamics with finite-element multibody procedures. Math Comput Model 33(10–11):1113–1137. https://doi.org/10.1016/S0895-7177(00)00303-4
22. Saberi H, Khoshlahjeh M, Ormiston RA, and Rutkowski MJ (2004) Overview of RCAS and application to advanced rotorcraft problems. In: Proceedings of the AHS 4th decennial aeromechanics specialists' conference, San Francisco, CA
23. Hodges DH (1990) A mixed variational formulation based on exact intrinsic equations for dynamics of moving beams. Int J Solids Struct 26(11):1253–1273
24. Im B, Cho H, Kee Y, Shin S (2020) Geometrically exact beam analysis based on the exponential-map finite rotations. Int J Aeronaut Space Sci 21(1):153–162
25. Araghizadeh MS, Sengupta B, Lee H, Myong RS (2024) Aeroacoustic investigation of side-by-side urban air-mobility aircraft in full configuration with ground effect. Phys Fluids 36(8):087106
26. Sengupta B, Araghizadeh MS, Lee H, Lee DJ (2024) Comparative analysis of direct and fast-multipole methods for multirotor wake dynamics. Int J Aeronaut Space Sci 25:1–20
27. Katz J, Plotkin A (2001) Low-speed aerodynamics, 2nd edn. Cambridge University Press, Cambridge, U.K.
28. Leishman GJ (2006) Principles of helicopter aerodynamics, 2nd ed. Cambridge University Press, New York
29. Lee H, Sengupta B, Araghizadeh MS, Myong RS (2022) Review of vortex methods for rotor aerodynamics and wake dynamics. Adv Aerodyn 4:20
30. Lee H, Lee DJ (2020) Rotor interactional effects on aerodynamic and noise characteristics of a small multirotor unmanned aerial vehicle. Phys Fluids 32(4):043105
31. Jung SU, Kwak DI, Kim SH, Choi JH, Shim DS (2013) Vibration reduction devices for the Korean utility helicopter. J Korean Soc Aeronaut Space Sci 41(12):987–993

32. Smith LR, Jones AR (2019) Measurements on a yawed rotor blade pitching in reverse flow. Phys Rev Fluids 4(3):034703
33. Lee H, Lee DJ (2019) Numerical investigation of the aerodynamics and wake structures of horizontal axis wind turbines by using nonlinear vortex lattice method. Renew Energy 132:1121–1133